catalysts

MDPI

Article

Efficient CO_2 Electroreduction on Tin Modified Cuprous Oxide Synthesized via a One-Pot Microwave-Assisted Route

Juqin Zeng [1,*], Marco Fontana [1], Micaela Castellino [2], Adriano Sacco [1], M. Amin Farkhondehfal [1], Filippo Drago [3] and Candido Fabrizio Pirri [1,2]

[1] Center for Sustainable Future Technologies @POLITO, Istituto Italiano di Tecnologia, Via Livorno 60, 10144 Turin, Italy; marco.fontana@iit.it (M.F.); adriano.sacco@iit.it (A.S.); amin.farkhondehfal@iit.it (M.A.F.); fabrizio.pirri@iit.it (C.F.P.)

[2] Department of Applied Science and Technology, Politecnico di Torino, C.so Duca degli Abruzzi 24, 10129 Turin, Italy; micaela.castellino@polito.it

[3] NanoChemistry, Istituto Italiano di Tecnologia, Via Morego 30, 16163 Genoa, Italy; Filippo.Drago@iit.it

* Correspondence: juqin.zeng@iit.it

Abstract: Bimetallic copper-tin catalysts are considered cost-effective and suitable for large-scale electrochemical conversion of CO_2 to valuable products. In this work, a class of tin (Sn) modified cuprous oxide (Cu_2O) is simply synthesized through a one-pot microwave-assisted solvothermal method and thoroughly characterized by various techniques. Sn is uniformly distributed on the Cu_2O crystals showing a cube-within-cube structure, and CuSn alloy phase emerges at high Sn contents. The atomic ratio of Cu to Sn is found to be crucially important for the selectivity of the CO_2 reduction reaction, and a ratio of 11.6 leads to the optimal selectivity for CO. This electrode shows a high current density of 47.2 mA cm^{-2} for CO formation at −1.0 V vs. the reversible hydrogen electrode and also displays good CO selectivity of 80–90% in a wide potential range. In particular, considerable CO selectivity of 72–81% is achieved at relatively low overpotentials from 240 mV to 340 mV. During the long-term tests, satisfactory stability is observed for the optimal electrode in terms of both electrode activity and CO selectivity. The relatively low price, the fast and scalable synthesis, and the encouraging performance of the proposed material implies its good potential to be implemented in large-scale CO_2 electrolyzers.

Keywords: carbon dioxide conversion; electrocatalysis; cuprous oxide; tin; overpotential

Citation: Zeng, J.; Fontana, M.; Castellino, M.; Sacco, A.; Farkhondehfal, M.A.; Drago, F.; Pirri, C.F. Efficient CO_2 Electroreduction on Tin Modified Cuprous Oxide Synthesized via a One-Pot Microwave-Assisted Route. *Catalysts* **2021**, *11*, 907. https://doi.org/10.3390/catal11080907

Academic Editor: Bruno Fabre

Received: 2 July 2021
Accepted: 23 July 2021
Published: 27 July 2021

1. Introduction

Electrochemical conversion of carbon dioxide (CO_2) can create a bridge between the carbon capture/storage process and the renewable energy technology. By utilizing clean electricity as energy input and captured CO_2 as raw material, the CO_2 reduction reaction (CO_2RR) can directly produce valuable chemical feedstocks, including C_1 products such as carbon monoxide (CO), methane (CH_4), methanol (CH_3OH), and formic acid (HCOOH), C_2 products such as ethylene (C_2H_4), ethane (C_2H_6) and ethanol (C_2H_5OH), C_{2+} products such as n-propanol ($CH_3CH_2CH_2OH$) and so on [1]. Among these products, the simple and small building-block molecules, CO and HCOOH, are considered to be techno-economic convenient and comparable with the conventional chemical synthesis [2]. CO plays a vital role in the chemical industry and is considered to be the most important and versatile C_1-building block [3]. Its utilization is intensive in processes such as Fischer-Tropsch synthesis of hydrocarbons and Monsanto/Cativa acetic acid synthesis at large industrial scales [4].

A tremendous effort has been dedicated to the CO_2RR, mainly focusing on the catalyst materials and processes [5,6]. State-of-the-art catalysts for the CO_2RR to CO are gold (Au) and silver (Ag), allowing excellent selectivity of over 95% [7,8]. Other materials, such as palladium (Pd), zinc (Zn), metal (Ni, Zn, Sb, and Co)-nitrogen-carbon complexes and copper alloys, also showed satisfactory CO selectivity [5,9,10]. Bimetallic Cu-Sn catalysts

have attracted the most intensive attention due to the high selectivity and good stability for the CO_2RR to CO in aqueous electrolyte [11–15]. In addition, compared with Au and Ag, Cu and Sn are much more abundant and more cost-effective, making Cu-Sn catalysts more suitable for the large-scale implementation. Hence, further study on the Cu-Sn catalysts is expected to bring benefits to both the academic and industrial sectors related to the CO_2 valorization. In most previous works, Cu-Sn catalysts were obtained by deposition methods and tested as free-standing electrodes in a batch reactor [11–17]. Despite the outstanding selectivity for the CO_2RR to CO, these free-standing electrodes suffer from severe mass diffusion limitations at relatively higher current densities (>15 mA cm^{-2}), making it commercially unfeasible [6]. One of the critical causes is the low solubility and diffusivity of CO_2 in aqueous electrolytes [18]. The electrolysis process with gas-fed CO_2 in a flow reactor is considered an effective strategy to mitigate the CO_2 transport limitation, resulting in current densities as high as tens to hundreds of milliamperes. In such an approach, the gas diffusion electrode (GDE) is the key component [19,20]. It is usually composed of a catalyst layer and a hydrophobic substrate. The high porosity and hydrophobicity of the GDE can ensure high CO_2 diffusion rates and shorten the diffusion distance from the substrate to the catalyst layer.

To enable the fabrication of GDEs, we fabricated a class of Sn-Cu material through a simple microwave-assisted solvothermal route, using tin acetate and copper acetate as Sn and Cu precursors, respectively. Ethylene glycol (EG) was used as both the solvent and the reducing agent. The Sn modified Cu_2O catalyst containing a nominal Cu:Sn atomic ratio of 12.0 is denoted as Sn-Cu_2O, and it is characterized by good CO selectivity (70–80%) at low overpotentials (240–340 mV) and encouraging performance in a wide potential range for the CO_2RR. Various samples with different atomic ratios of Cu to Sn have been synthesized and studied for comparison and they are denoted as CuSn0.5, CuSn1.0, and CuSn2.0 with nominal Cu:Sn ratios of 36.0, 18.0, and 9.0, respectively.

2. Results and Discussion

2.1. Physical and Chemical Characterizations of the As-Prepared Catalysts

X-ray diffraction (XRD) analysis was firstly performed to study the crystalline phase composition of the samples. As shown in Figure 1a, the peaks of the Cu_2O sample correspond to the reflections related to the (110), (111), (200), (211), (220), (311), and (222) planes of crystalline Cu_2O (cubic, space group Pn-3m) [21]. No peaks for impure crystalline phases are observed for this sample. The Sn-Cu_2O sample shows a similar XRD pattern with peaks for only Cu_2O phase (Figure 1b). However, careful inspection of the pattern reveals a clear shoulder in the (200) peak (see Figure 1c). In the literature, some CuSn alloys with various stoichiometry show XRD patterns that mainly consist of only one dominant peak in the 42–43° 2θ range [22,23]. Other samples with different Cu:Sn atomic ratios have also been characterized by XRD. As shown in Figure S1, the samples with lower Sn contents show only crystallline Cu_2O phase, and the sample which contains more Sn also displays a CuSn alloy peak in the 42–43° 2θ range at notable intensity.

In order to gain further insight into the crystalline structure of both samples, the XRD patterns are fitted by Rietveld refinement using the structural models reported in the experimental section, and the refined parameters are shown in Table 1. It is interesting to note that there is no significant change in the lattice parameter and the coherent scattering domain size for the Cu_2O phase in both samples. Concerning the Sn-Cu_2O sample, this outcome means that eventual incorporation of Sn atoms in the Cu_2O phase (thus labeled Cu_2O:Sn) is not causing distortion of the unit cell if we assume that the Sn content is not limited only to the CuSn alloy phase.

The morphology and particle size of the as-prepared catalysts were studied by Field emission scanning electron microscopy (FESEM). As shown in Figure 2a,b, the Cu_2O sample is composed of flower-like particles that resemble eight-petal-shaped crystals. Four petals are present in each plane and are highly symmetric in the structure. This eight-pod framework is likely due to the crystal branching along all ⟨111⟩ directions of Cu_2O [24].

Similar branching was also observed in ethanol-water solvents with formic acid as the reducing agent [25]. In some particles, the pods are significantly amplified and each pod has a cubic shape. These particles tend to form a big cube and they are called "cube-within-cube" or "crystal-within-crystal" arrangements [25]. Some particles eventually grow into single symmetric cubes with a small space in the center, due to the faster growth of the eight petals. The addition of a small number of Sn^{4+} ions leads to faster growth of the eight petals into small cubes that are packed in a cubic aggregate, as shown in Figure 2d,e. In most particles, the center space is significantly narrowed and even eliminated, generating single symmetric cubes. Despite the difference in the morphology, most particles in both samples show a similar average particle size of 8–10 µm and have a rough surface (Figure 2c,f). Moreover, it is worth noting the presence of a second class of structures with irregular lamellar morphology, with variable lateral size in the micrometer range.

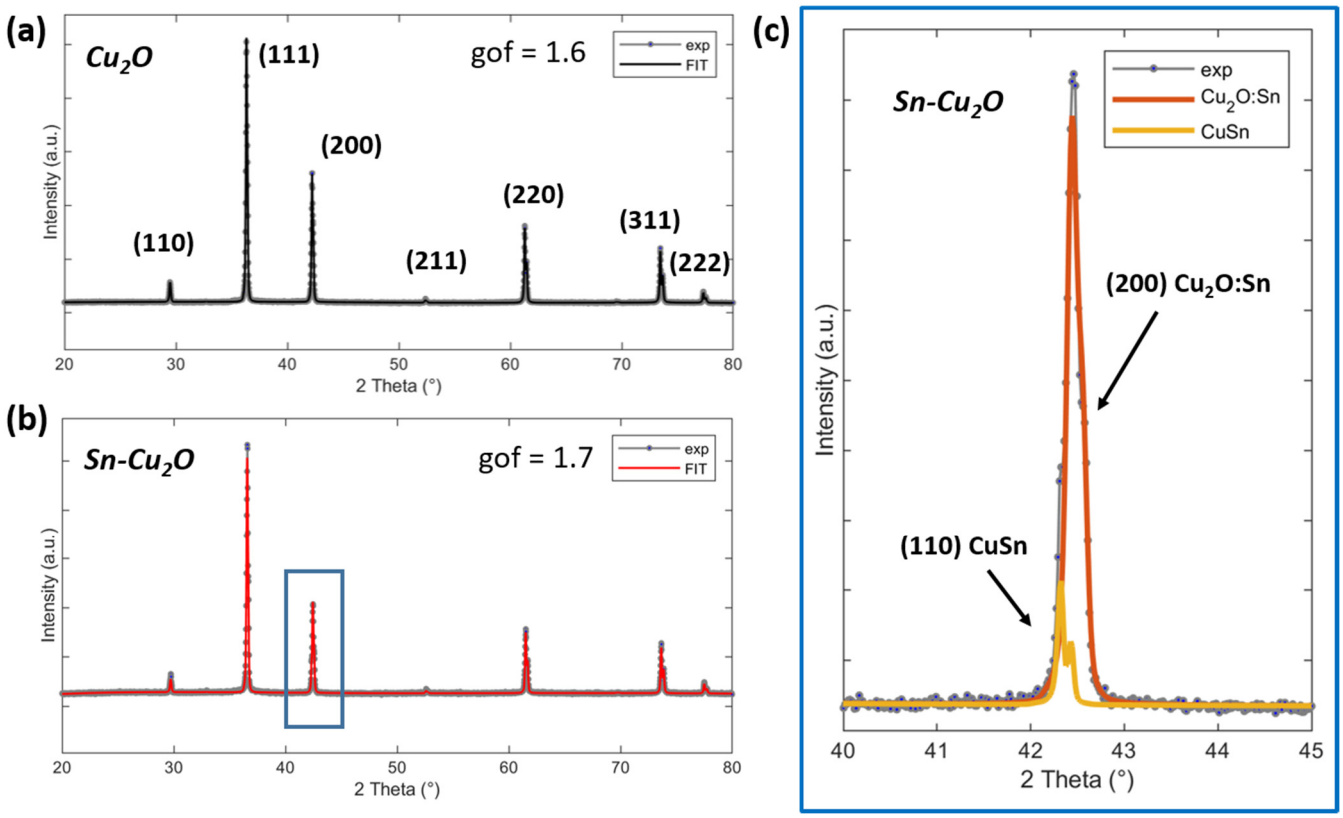

Figure 1. XRD patterns of Cu_2O (**a**) and Sn-Cu_2O (**b**) catalysts with corresponding Rietvled refinement fit and goodness-of-fit (gof) values. Panel (**c**) provides a view of the (200) peak of the XRD pattern from Sn-Cu_2O sample, showing contributions from two different phases.

Table 1. Parameters obtained from Rietveld refinement for the Cu_2O and Sn-Cu_2O samples.

Cu_2O				Sn-Cu_2O			
Phase	**Cu_2O**	**a (Å)**	**Size (nm)**	**Phase**	**Cu_2O:Sn**	**a (Å)**	**Size (nm)**
-	cubic	4.268	108	-	cubic	4.269	88
-	*Pn-3m*	-	-	-	*Pn-3m*	-	-
-	-	-	-	-	-	-	-
-	-	-	-	phase	CuSn	a (Å)	size (nm)
-	-	-	-	-	cubic	3.027	285
-	-	-	-	-	*Im-3m*	-	-

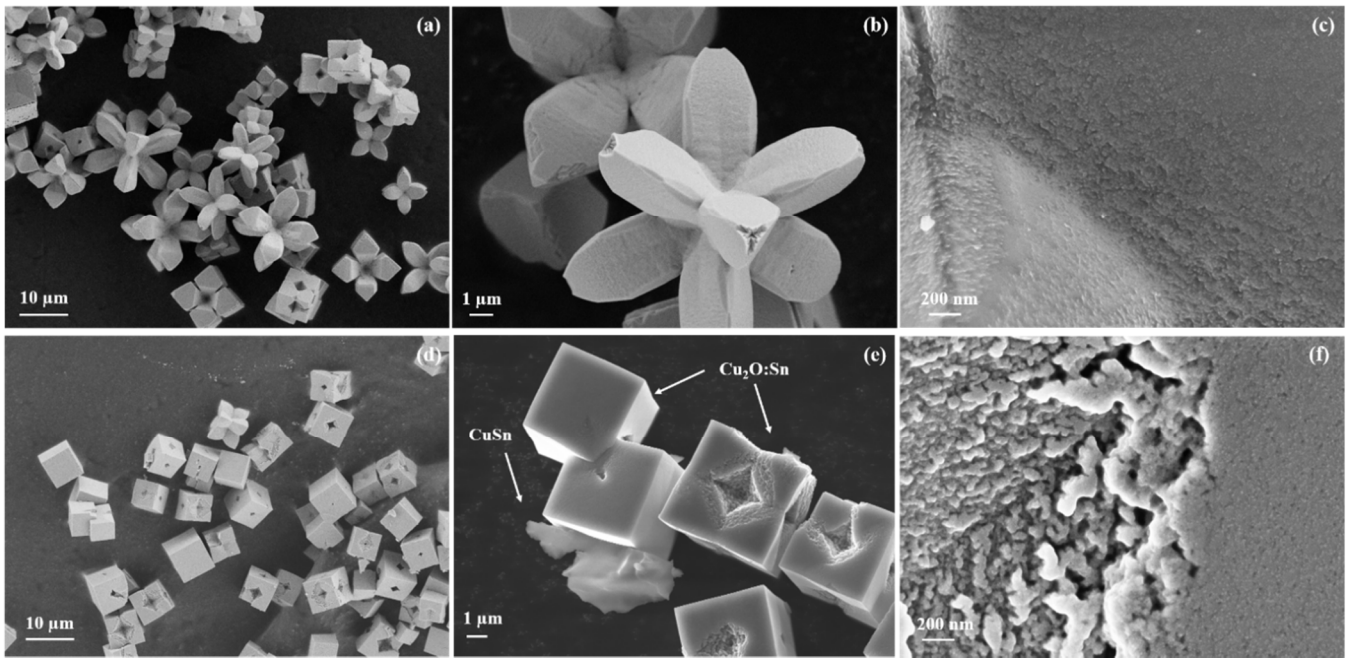

Figure 2. FESEM images of the samples. (**a**–**c**) Cu_2O, (**d**–**f**) Sn-Cu_2O.

Energy dispersive X-ray (EDX) analysis provides useful information on these two classes of structures, as shown in Figure S2. Specifically, EDX mapping proves two important points: (1) Sn is homogeneously distributed in both cubic and lamellar structures; (2) a higher Sn/Cu at % ratio is present in the lamellar structures. Combining EDX and XRD results, it is reasonable to ascribe the Cu_2O:Sn crystalline phase to the cubic morphology, while the CuSn crystalline phase is associated with the lamellar structures with a higher Sn content.

FESEM analysis has also been performed on other samples with various Cu:Sn ratios, as shown in Figure S3. It is likely that a higher Sn^{4+} concentration in the precursor solution promotes the growth of the eight petals into an entire cube. In addition, the sample with the highest Sn content (Cu:Sn = 9.0) shows significant irregular and lamellar structures associated with the CuSn alloy phase, in agreement with the XRD result (Figure S1).

Inductively coupled plasma optical emission spectrometry (ICP-OES) analysis was performed in order to quantify the Cu and Sn elements. It is found that the Cu_2O sample contains 85 wt.% of Cu element, and the Sn-Cu_2O sample consists of 70 wt.% of Cu and 11 wt.% of Sn. By stoichiometric calculation, the Cu_2O percentage is 96 wt.% in the Cu_2O sample, and the Sn-Cu_2O sample contains 79 wt.% of Cu_2O and 11 wt.% of Sn (about 14 wt.% of O-Sn-O). The atomic ratio of Cu to Sn is calculated to be 11.6, which is in good agreement with the nominal one of 12.0 in the precursor solution. The remaining weight could be attributed to the surface adsorbed species. By ICP analysis, it is further confirmed that other samples with various Cu:Sn ratios are composed of the desired Cu and Sn contents.

X-ray photoelectron spectroscopy (XPS) measurements have been performed on Cu_2O and Sn-Cu_2O samples in order to examine their surface physicochemical properties. From surveys spectra in Figure 3a, we can verify the presence of Cu, O, and C on both samples and the Sn signal only from the Sn-Cu_2O one. C1s peak, on both samples, is mainly due to the environmental exposure (spectra not reported). From the HR spectra, we can distinguish different oxidation states, thanks to the evaluation of chemical shifts in the binding energy (BE) scales. From Cu2p HR doublets (Figure 3b), we can clearly see that both samples show typical spectra related to Cu^+ oxidation state, with a very small and weak satellite due to Cu^{2+} state [26]. To further confirm this attribution, we also checked the $CuL_3M_{4.5}M_{4.5}$ Auger peaks, from which the modified Auger parameter can

be calculated [27]. This parameter also allows us to distinguish between Cu^+ and Cu^0, which show almost the same chemical shift in the Cu2p doublet. We thus obtained two values equal to 1849.3 eV and 1849.4 eV for Cu_2O and Sn-Cu_2O samples, respectively, in accordance with the reported value of 1849.2 ± 0.3 eV for Cu^+ average oxidation state [26]. A final check has been reserved to the Sn3d doublet for Sn-Cu_2O sample (Figure 3d). A typical spectrum due to Sn^{2+} oxidation state is clearly observed [12], with $Sn3d_{5/2}$ peak located at 486.3 eV and its counterpart $Sn3d_{3/2}$ at 494.7 eV ($\Delta_{doublet}$ = 8.4 eV).

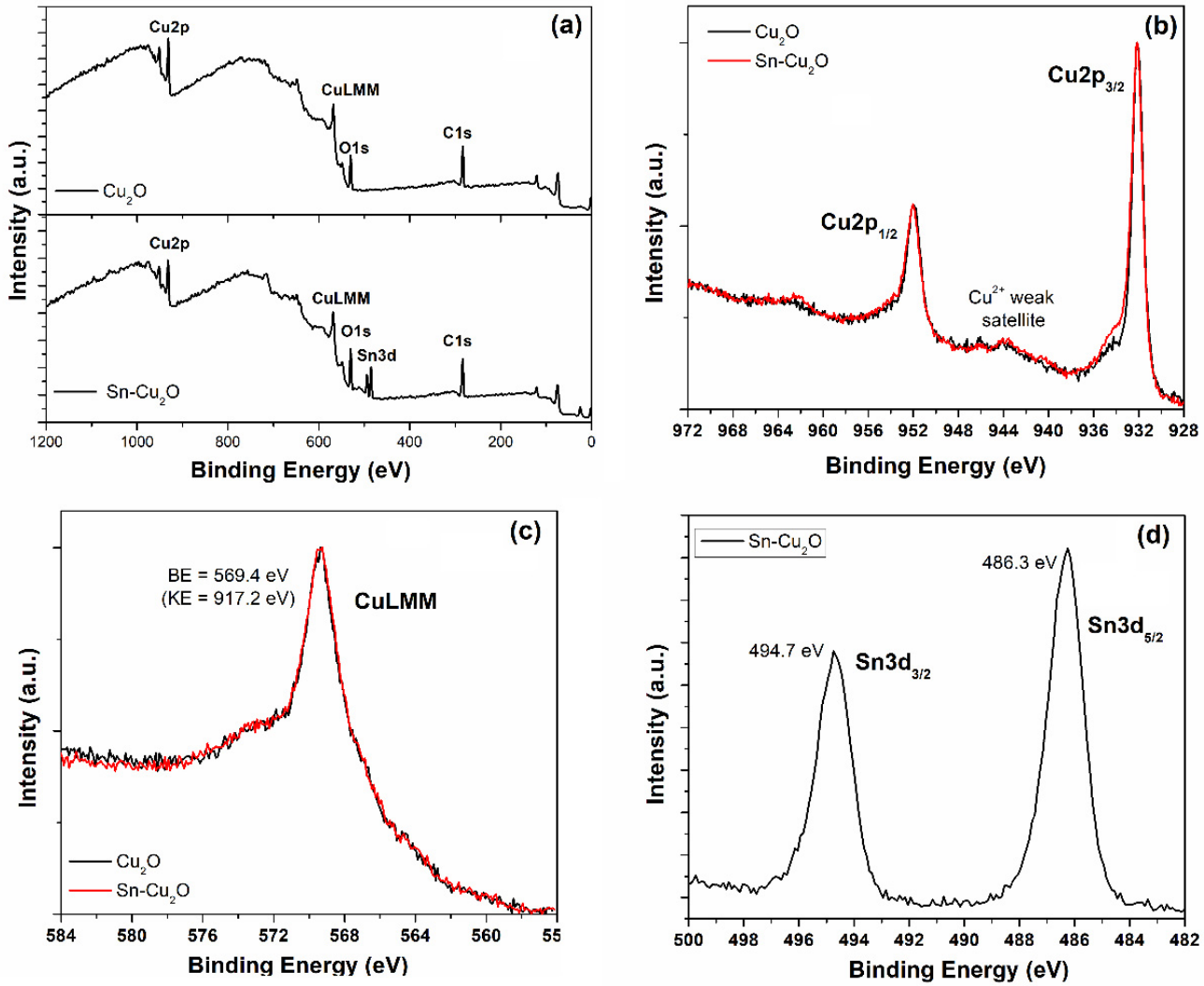

Figure 3. XPS analyses on the prepared samples: (**a**) survey spectra, (**b**) Cu2p doublet HR spectra, (**c**) $CuL_3M_{4.5}M_{4.5}$ Auger peaks, and (**d**) Sn3d doublet HR spectrum.

2.2. Comparison of the CO_2RR Performance on Various Samples

In order to compare the activity and selectivity of Cu_2O and Cu-Sn materials for the CO_2RR, chronoamperometric (CA) measurements were carried out in a batch cell (Scheme S1a) in a CO_2-saturated 0.1 M $KHCO_3$ solution. All potentials are reported versus the reversible hydrogen electrode (RHE) in this work. The i-t curves and product analyses are shown in Figure 4. At each potential, the Cu_2O electrode (Figure 4a) shows a higher current density than the Sn-Cu_2O one (Figure 4c). On both electrodes, the current density increases while negatively shifting the applied potential. In the investigated potential range, the Cu_2O electrode shows poor selectivity for the CO_2RR, with faradaic efficiency for CO (FE_{CO}) lower than 7% and FE_{HCOOH} smaller than 15% (Figure 4b). In contrast, the Sn-modified Cu_2O sample shows significantly enhanced CO_2RR selectivity, with CO as

the dominant product (Figure 4d). The CO selectivity reaches a good value of about 87% at −0.6 V and −0.7 V, and it decreases at −0.8 V and −0.9 V. The partial current densities for CO formation (j_{CO}) are calculated to be 1.3 mA cm^{-2}, 2.0 mA cm^{-2}, 3.0 mA cm^{-2}, and 3.7 mA cm^{-2} at −0.6 V, −0.7 V, −0.8 V, and −0.9 V, respectively, which are typically low at such potentials in a batch reactor [4,11,28]. The CO_2RR performance of other samples with various Cu:Sn ratios is shown in Figure S4. A very low amount of Sn addition (Cu:Sn = 36.0) can significantly increase the CO selectivity of the Cu_2O electrode, and the CO selectivity is enhanced with further increase of the Sn content until the Cu:Sn reaches about 12.0 in the Sn-Cu_2O. Further raising the Sn amount leads to the decrease of CO selectivity and the increase of HCOOH selectivity. Hence, the Sn-Cu_2O sample is optimal for the CO_2RR to CO in this study.

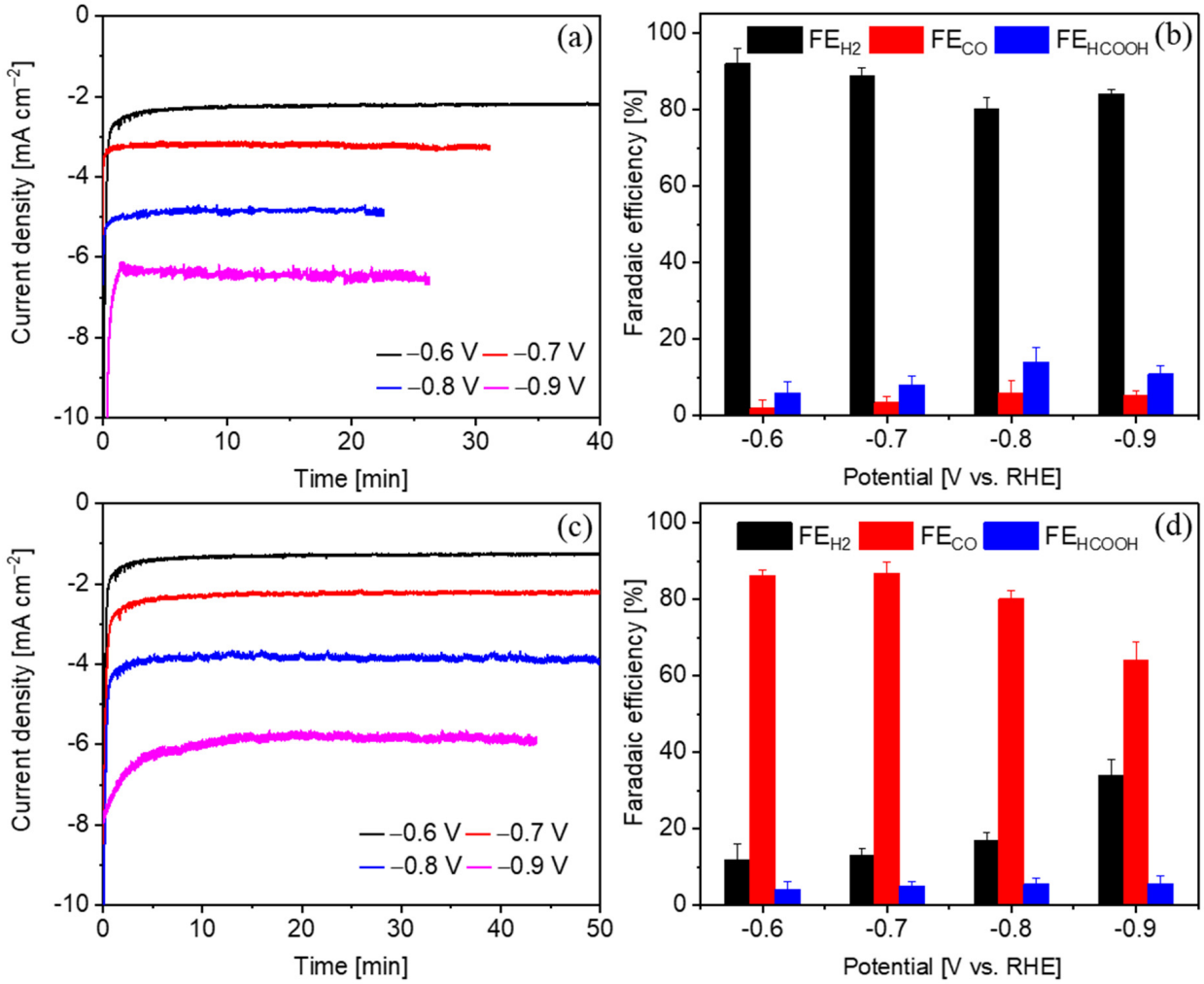

Figure 4. CA measurements and product analyses in a CO_2-saturated 0.1 M $KHCO_3$ aqueous solution in a batch cell. (**a**) i-t curves at various potentials on Cu_2O electrode and (**b**) the corresponding product analyses, (**c**) i-t curves at various potentials on Sn-Cu_2O electrode and (**d**) the corresponding product analyses.

Many studies have explored the role of Sn in the CO_2RR and the electronic properties of the Cu-Sn bimetallic materials by density functional theory (DFT) calculation. Qiao et al. reported that Sn can donate electrons to Cu, causing the charge redistribution on the surface [29]. The Sn sites that are positively charged can hinder nucleophilic attack on the carbon atoms, increasing the thermodynamic barrier to *COOH adsorption. Hence, a high Sn content can promote the formation of HCOOH. However, a large amount of works demonstrate that a relatively low Sn percentage prefers to produce CO [11–14]. Wang et al. [30] reported that the increased electron density on the Cu sites, assisted by

the adjacent SnO_x sites, can weaken the binding of *CO, and thus can favor the CO_2RR to CO. Takanabe et al. [11] suggested that H adsorption on the Sn modified Cu facets is much lower compared to that on the pure Cu structure, explaining the high selectivity for the CO_2RR on the Sn modified Cu materials. These results suggest that Sn modification can increase the CO_2RR selectivity of Cu, and a high amount of Sn in the Cu-Sn materials favors the production of HCOOH, while a relatively low Sn content prefers the CO formation, in good agreement with the results presented herein.

2.3. Study of the CO_2RR on the Sn-Cu_2O Electrode in a Semi-Flow Cell

Further investigations have been carried out at the Sn-Cu_2O electrode in a semi-flow cell fed with gas phase CO_2. In 0.1 M $KHCO_3$, the Sn-Cu_2O electrode performs better in a flow cell (Figure 5a) than in a batch cell (Figure 4c,d) in terms of both the reaction rate and the selectivity toward the CO_2RR to CO. The FE_{CO} is about 45% at −0.35 V and it becomes dominant at lower potentials. It reaches 79% at −0.45 V and surpasses 80% from −0.5 V to −1.0 V. The FE_{CO} is peaked at about 90% from −0.6 V to −0.8 V. The j_{CO} is 1.8 mA cm^{-2} at −0.6 V and it rapidly increases to 9.9 mA cm^{-2} at −0.9 V. The total current densities are 2.0 mA cm^{-2}, 3.5 mA cm^{-2}, 5.5 mA cm^{-2}, and 12.2 mA cm^{-2} at −0.6 V, −0.7 V, −0.8 V, and −0.9 V, respectively, which are much higher than those obtained in the batch cell and are superior to the reported results at similar test conditions [12,14]. In addition, no significant CO_2 diffusion limitation has been observed in the flow cell since the CO formation rate increases rapidly with raising the electrochemical driving force even at very negative potentials. More concentrated $KHCO_3$ electrolytes have further been utilized for the CO_2RR on the Sn-Cu_2O electrodes. The HCO_3^- ions can not only enhance the ionic conductivity, but also increase the local CO_2 availability near the electrode surface [31,32]. As shown in Figure 5 and Table S1, the partial current density for CO formation increases with raising the $KHCO_3$ concentration at each potential, particularly at more negative ones ($\leq$−0.8 V). The CO formation rate raises with negatively shifting the potential in each electrolyte and it reaches a highest current density of 47.2 mA cm^{-2} at −1.0 V in 2.0 M electrolyte. No CO_2 diffusion limitation is noticed, indicating that the CO_2 availability is indeed enhanced in the flow cell with respect to that in the batch one. The CO selectivity of the electrode is also affected by the $KHCO_3$ concentration. As displayed in Figure 5 and Table S2, the FE_{CO} shows a higher value in the 0.1 M $KHCO_3$ electrolyte compared to those obtained in other concentrations at most of the low potentials ($\leq$−0.5 V). At higher potentials (>−0.5 V), the electrolyte with 1.0 M $KHCO_3$ leads to the highest CO selectivity with FE_{CO} values of 72%, 79%, and 81% at −0.35 V, −0.4 V, and −0.45 V, respectively. Such potentials are more positive than the reported ones where similar CO selectivity was obtained in the literatures [11–14,33–36]. It is further worth noticing that the CO_2RR performance of the Sn-Cu_2O electrode represents one of the best outcomes among those obtained with CuSn-based electrocatalysts recently proposed in the literatures for the CO_2 conversion to CO (see Table S3).

The stability of the Sn-Cu_2O electrode has been evaluated in various CO_2-saturated $KHCO_3$ electrolytes, as shown in Figure 6. At relatively low current density (<10 mA cm^{-2}), the electrode displays very good stability in terms of both reactivity and CO selectivity (Figure 6a,b). As the $KHCO_3$ concentration in the electrolyte increases, the current density increases and its retention during the long-term electrolysis remains excellent, while the CO selectivity slightly decreases as a function of time (Figure 6c,d). Nevertheless, at the end of 10-h tests, the CO selectivity retains good values of about 90% in the 0.1 M and 0.5 M $KHCO_3$ electrolytes and 80% and 70% in the 1.0 M and 2.0 M electrolytes, respectively.

Concisely, the Sn-Cu_2O electrode shows good activity and selectivity for the CO_2RR to CO in a wide potential range. In particular, it achieves considerable CO selectivity at relatively low overpotentials from 240 mV to 340 mV. From the long-term tests, the Sn-Cu_2O demonstrates encouraging stability during the CO_2RR in various concentrated $KHCO_3$ electrolytes. Hence, it is possible to anticipate that the facilely synthesized material could be a promising candidate for the CO_2 valorization at large scales.

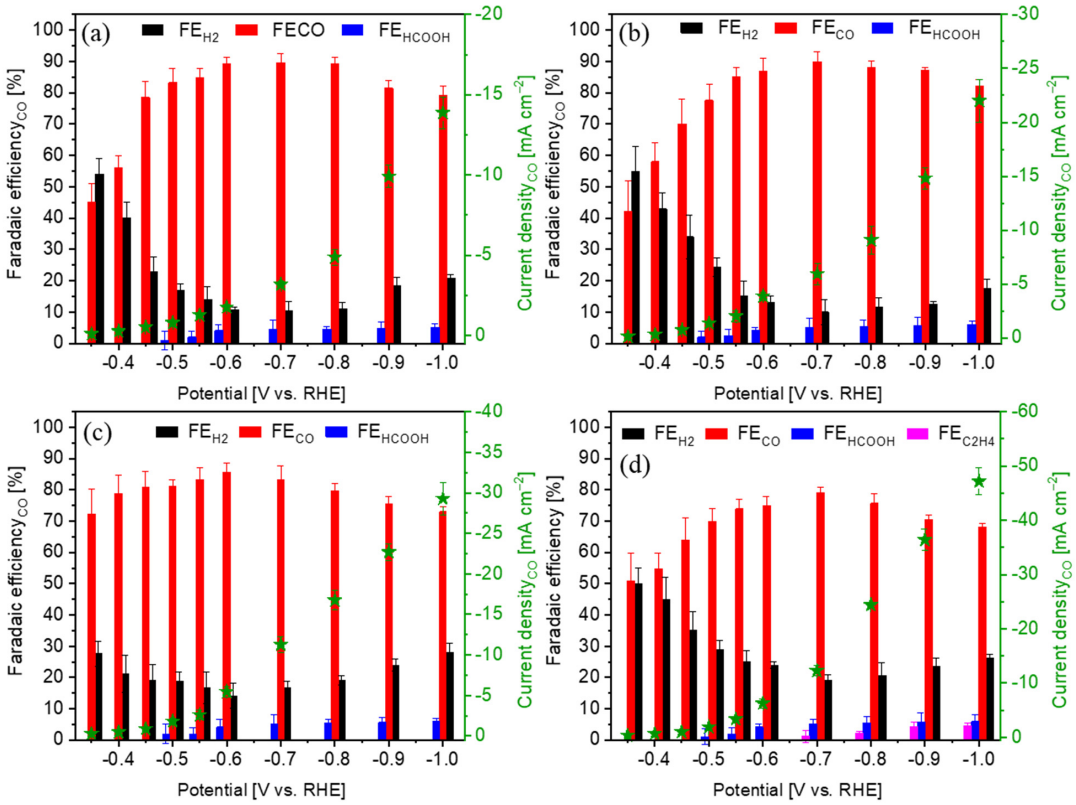

Figure 5. Product analyses and CO current density at a Sn-Cu_2O electrode in a semi-flow cell with various CO_2-saturated $KHCO_3$ electrolytes: (**a**) 0.1 M, (**b**) 0.5 M, (**c**) 1.0 M, and (**d**) 2.0 M.

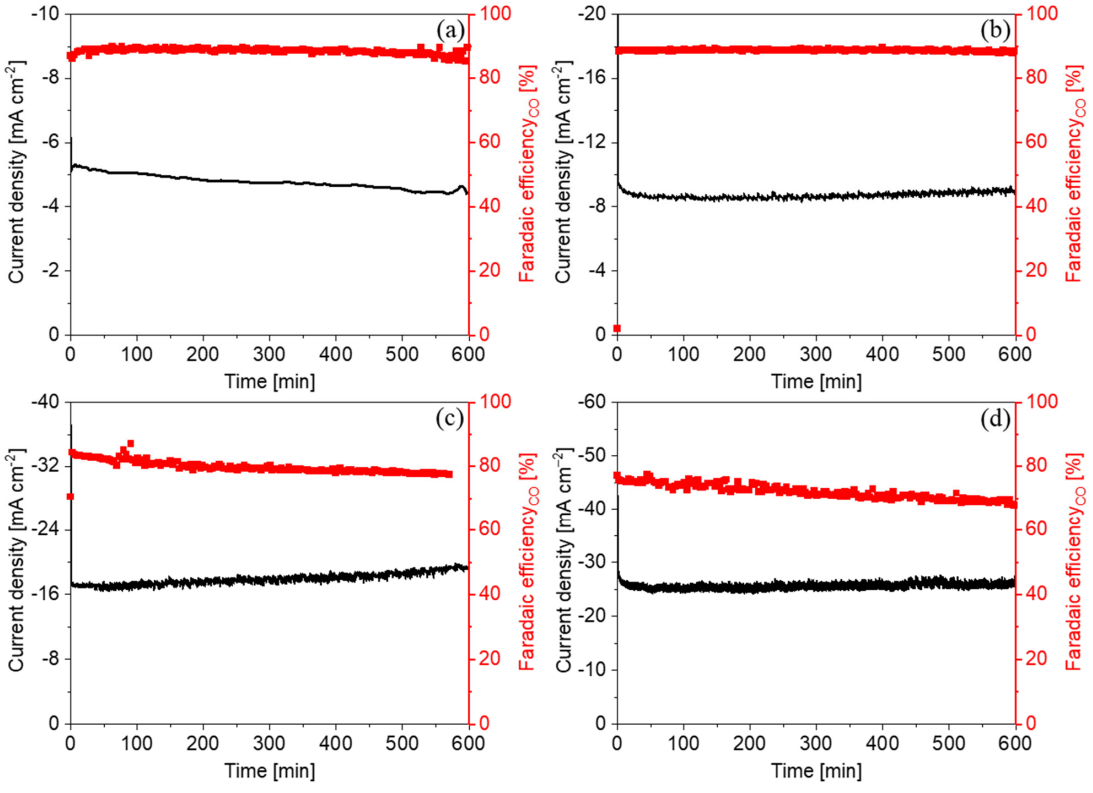

Figure 6. Geometric current density and CO selectivity at a Sn-Cu_2O electrode during 10-h tests in various CO_2-saturated $KHCO_3$ electrolytes: (**a**) 0.1 M, (**b**) 0.5 M, (**c**) 1.0 M and (**d**) 2.0 M.

3. Materials and Methods

3.1. Materials

Nafion® 117 solution (5 wt.%), isopropanol, copper(II) acetate ($Cu(CH_3COO)_2$, 99.9%), tin(IV) acetate ($Sn(CH_3COO)_4$, 99.9%), sodium hydroxide (NaOH, 98%), potassium bicarbonate ($KHCO_3$, 99.7%), ethylene glycol (EG, 99.8%), and acetic acid (CH_3COOH, 99.8%, anhydrous) were purchased from Sigma-Aldrich (Merck, Germany). All the chemicals were used as received.

3.2. Synthesis

For the preparation of the Sn modified Cu_2O catalyst containing a nominal Cu:Sn atomic ratio of about 12.0 (denoted as Sn-Cu_2O), 150 mg of $Sn(CH_3COO)_4$ was dissolved in 2 mL of CH_3COOH. Meanwhile, 920 mg of $Cu(CH_3COO)_2$ was dissolved in 40 mL EG and 5 mL of H_2O. Then, the $Sn(CH_3COO)_4$ solution was added into $Cu(CH_3COO)_2$ solution drop by drop. After vigorous agitation for 5 min, the mixture was transferred into a microwave oven (Milestone STARTSynth, Milestone Inc., Italy). The irradiation lasted for 2 min at 900 W with a $T_{Max.}$ of 220 °C. After cooling down to room temperature, the precipitate was separated by centrifuge, washed twice with H_2O and once with ethanol, and then dried at 60 °C overnight under vacuum. Other samples with different atomic ratios of Cu to Sn, namely CuSn0.5, CuSn1.0, and CuSn2.0 with a Cu:Sn ratio of 36.0, 18.0, and 9.0, respectively, were prepared for comparison by changing the amounts of precursors. The Cu_2O sample was also prepared with the same procedure except that the precursor solution was 920 mg of $Cu(CH_3COO)_2$ dissolved in 40 mL of EG, 2 mL of CH_3COOH, and 5 mL of H_2O.

3.3. Physical and Chemical Characterizations

ICP-OES, with an iCAP 7600 DUO (Thermo Fisher Scientific, Waltham, MA, USA), was used to analyze the Cu and Sn elements.

The crystalline phases of the powder samples were analyzed by XRD measurements, which were performed on a PANalytical X'Pert Pro instrument (Cu-Kα radiation, 40 kV and 30 mA) with a PANalytical X'Celerator detector. The XRD patterns were analyzed by means of Rietveld refinement with the software TOPAS-Academic [37]. The structural model used for Cu_2O is Crystallography Open Database (COD) ID: 9007497, while for the CuSn the reference model is COD ID: 1524713. The diffractometer instrumental function was determined by analyzing the XRD pattern of the LaB_6 standard provided by the National Institute of Standards and Technology. Peak broadening due to coherent scattering domain size was modelled by using Gaussian and Lorentzian contributions implemented in the CS_G and CS_L functions in TOPAS-Academic.

To analyze the morphology of the materials, FESEM (ZEISS Auriga, Eggenstein-Leopoldshafen, Germany) was performed on the powder samples. EDX spectroscopy was carried out with an Oxford Instruments X-max detector based on Silicon drift technology with a 50 mm^2 active area.

XPS was performed on the powder samples to examine the surface compositions. A PHI 5000 VersaProbe (Physical Electronics, Chanhassen, MN, United States) system with an X-ray source of a monochromatic Al Kα radiation (1486.6 eV) was employed for the analysis and the spectra were analyzed with MultiPak Version 9.0 dedicated software. C1s peak at 284.5 eV was used as reference for all core-level peak energies and the background contribution was subtracted by means of a Shirley function in the high resolution (HR) spectra.

3.4. Electrode Preparation

For the fabrication of the electrode, 15 mg of a synthesized catalyst, 1.5 mg of acetylene carbon black (CB, Shawinigan Black AB50), 67.5 µL of Nafion® 117 solution, and 400 µL of isopropanol were mixed and sonicated for 40 min until a uniform slurry was obtained. The slurry was then casted onto a carbon paper with a microporous layer (GDL; SIGRACET

28BC, SGL Technologies, Germany). The obtained electrode was dried at room temperature overnight to evaporate the solvents. The catalyst loading of each electrode is approximately 3.0 mg cm^{-2}.

3.5. CO_2 Electrolysis and Product Analysis

The CO_2RR was performed by using chronoamperometric technique on a CHI760D potentiostat (CH Instruments, Inc., 3700 Tennison Hill Drive Austin, TX, USA). The potential was corrected by compensating the ohmic potential drop, of which 85% by the instrument (iR-compensation) and 15% by manual calculation.

For the comparison of various electrodes, CA experiments were conducted in a customized two-compartment three-electrode batch cell, as shown in Scheme S1a. A proton exchange membrane (Nafion™ Membrane N117, Ion Power, München, Germany) was used to separate the anodic and cathodic sides. The reference electrode was a mini Ag/AgCl (1 mm, leak-free LF-1) and the counter was a Pt foil. A catalyst-coated carbon paper (geometric area: 1.35 cm^2) was used as the working electrode. A 0.1 M $KHCO_3$ aqueous solution was used as the electrolyte for both sides. During the CA tests, a constant CO_2 flow was maintained at 15 mL min^{-1} to saturate the electrolyte and to bring out the gaseous products.

The Sn-Cu_2O electrode was then evaluated in a customized three-compartment three-electrode semi-flow cell, as shown in Scheme S1b. In the flow cell, the cathode separated the cathodic side into two compartments: one was the catholyte and the other was the CO_2 gas feed. Both catholyte and anolyte were 25 mL of $KHCO_3$ aqueous solution with the same concentration (0.1 M, 0.5 M, 1.0 M, or 2.0 M) and were circulated at 2 mL min^{-1} during the test. A constant CO_2 flow of 5 mL min^{-1} was purged through the anolyte in order to maintain a constant pH. A CO_2 flow of 15 mL min^{-1} was maintained in the gas compartment of the cathodic side in order to supply the CO_2 reactant and bring out the products.

A micro gas chromatograph (μGC, Fusion®, INFICON, Bad Ragaz, Switzerland) was used to analyze the gas-phase products in real time. The μGC was equipped with two modules, one with a 10 m Rt-Molsieve 5A column and the other with an 8 m Rt-Q-Bond column, and both with a micro thermal conductivity detector (micro-TCD). The products in liquid phase were detected through a high-performance liquid chromatograph (Thermo Scientific Ultimate3000 HPLC, Waltham, MA, United States). The detector was a UV-Vis one set at 210 nm and the column is a ReproGel (300 × 8 mm). An aqueous solution of 9.0 mM H_2SO_4 (flow rate of 1.0 mL min^{-1}) was used as the mobile phase.

Faradaic efficiency (FE), namely current efficiency, is the key parameter for determining the selectivity of the electrode toward a specific product. The FE for a specific product was calculated by applying Equation (1),

$$\mathrm{FE} = \frac{nNF}{Q} \tag{1}$$

where n is the number of electrons required to obtain 1 molecule of this product (n = 2 for CO, HCOOH, and H_2 formation); N is the amount of an identified product (number of moles, mol); Q is the total charge passed through the system during the electrolysis (coulombs, C); F is the Faraday constant (96,485 C mol^{-1}).

Partial current density for CO formation, j_{CO}, was calculated via Equation (2),

$$j_{co} = j_{total} * FE_{CO} \tag{2}$$

where FE_{CO} is the FE for CO formation and j_{total} is the total geometric current density.

The production rate of CO (μmol h^{-1} cm^{-2}) was calculated through Equation (3),

$$Production\ rate_{co} = \frac{j_{CO} * t}{2F} * 10^3 \tag{3}$$

where t is a constant of 3600.

4. Conclusions

In this work, powder-like Sn-Cu bimetallic materials have been synthesized and studied for the electrochemical CO_2 conversion. Assisted by microwave, the solvothermal synthesis process was found to be fast, simple, and energetically convenient. All obtained powder samples are mainly composed of Cu_2O crystals that are uniformly modified by Sn, and some of them with high Sn contents also consist of a CuSn alloy. The catalytic performance of the optimal Sn-Cu_2O electrode toward the CO_2RR has been investigated in $KHCO_3$ electrolyte with various concentrations, showing good selectivity, activity, and stability. Based on the encouraging results, future work will be focused on the improvement of the GDEs in order to further increase the CO_2 conversion rate and the CO selectivity, aiming at facilitating the application of the herein proposed material in the large-scale electrosynthesis of valuable chemicals from CO_2 feedstock.

Supplementary Materials: The following are available online at https://www.mdpi.com/article/10.3390/catal11080907/s1. Scheme S1: Electrochemical cells for the CO_2 electrolysis: (a) batch cell and (b) semi-flow cell. Figure S1: XRD patterns of Cu_2O, CuSn0.5, CuSn1.0 and CuSn2.0 samples (a) and a view of (200) peak (b). Figure S2: EDX characterization of the region of sample Sn-Cu_2O depicted in the FESEM image, consisting of an EDX spectrum, Cu Kα and Sn Lα elemental maps. Figure S3: FESEM images of the samples. (a) Cu_2O, (b) CuSn0.5, (c) CuSn1.0, (d) Sn-Cu_2O and (e) CuSn2.0. Figure S4: CO_2RR in a batch cell in a CO_2-saturated 0.1 M $KHCO_3$ aqueous solution on various samples. The dark green line is a guide to the eye for CO partial current density. Table S1: Current density for CO formation on the Sn-Cu_2O electrode at various potentials in different electrolytes. Table S2: Faradaic efficiency for CO formation on the Sn-Cu_2O electrode at various potentials in different electrolytes. Table S3: Comparison of different CuSn-based electrocatalysts in liquid-phase CO_2 electrolysis.

Author Contributions: Resources, C.F.P.; conceptualization, J.Z.; methodology, J.Z., M.F. and M.C.; investigation, J.Z., M.F., M.C., M.A.F. and F.D.; data curation, J.Z., M.F. and M.C.; writing—original draft preparation, J.Z., M.F. and M.C.; writing—review and editing, J.Z., M.F., M.C., M.A.F., F.D. and A.S.; validation, J.Z., M.F., M.C., M.A.F., A.S., F.D. and C.F.P. All authors have read and agreed to the published version of the manuscript.

Funding: This research did not receive any specific grant from funding agencies in the public, commercial, or not-for-profit sectors.

Data Availability Statement: Data are contained within the article.

Conflicts of Interest: The authors declare no conflict of interest.

References

1. Kuhl, K.P.; Cave, E.R.; Abram, D.N.; Jaramillo, T.F. New insights into the electrochemical reduction of carbon dioxide on metallic copper surfaces. *Energy Environ. Sci.* **2012**, *5*, 7050–7059. [CrossRef]
2. Bushuyev, O.S.; De Luna, P.; Dinh, C.T.; Tao, L.; Saur, G.; Van de Lagemaat, J.; Kelley, S.O.; Sargent, E.H. What Should We Make with CO_2 and How Can We Make It? *Joule* **2018**, *2*, 1–8. [CrossRef]
3. Nielsen, D.U.; Hu, X.-M.; Daasbjerg, K.; Skrydstrup, T. Chemically and electrochemically catalysed conversion of CO_2 to CO with follow-up utilization to value-added chemicals. *Nat. Catal.* **2018**, *1*, 244–254. [CrossRef]
4. Zeng, J.; Rino, T.; Bejtka, K.; Castellino, M.; Sacco, A.; Farkhondehfal, M.A.; Chiodoni, A.; Drago, F.; Pirri, C.F. Coupled Copper-Zinc Catalysts for Electrochemical Reduction of Carbon Dioxide. *ChemSusChem* **2020**, *13*, 4128–4139. [CrossRef] [PubMed]
5. Hoang, V.C.; Gomes, V.G.; Kornienko, N. Metal-based nanomaterials for efficient CO_2 electroreduction: Recent advances in mechanism, material design and selectivity. *Nano Energy* **2020**, *78*, 105311. [CrossRef]
6. Burdyny, T.; Smith, W.A. CO_2 reduction on gas-diffusion electrodes and why catalytic performance must be assessed at commercially-relevant conditions. *Energy Environ. Sci.* **2019**, *12*, 1442–1453. [CrossRef]
7. Hossain, M.N.; Liu, Z.; Wen, J.; Chen, A. Enhanced catalytic activity of nanoporous Au for the efficient electrochemical reduction of carbon dioxide. *Appl. Catal. B Environ.* **2018**, *236*, 483–489. [CrossRef]
8. Han, X.; Liu, L.; Yuan, J.; Zhang, X.; Niu, D. Polyacrylamide-Mediated Silver Nanoparticles for Selectively Enhancing Electroreduction of CO_2 towards CO in Water. *ChemSusChem* **2020**, *13*, 1–10. [CrossRef]

9. Koshy, D.M.; Chen, S.; Lee, D.U.; Stevens, M.B.; Abdellah, A.M.; Dull, S.M.; Chen, G.; Nordlund, D.; Gallo, A.; Hahn, C.; et al. Understanding the Origin of Highly Selective CO_2 Electroreduction to CO on Ni,N-doped Carbon Catalysts. *Angew. Chem. Int. Ed.* **2020**, *59*, 4043–4050. [CrossRef]
10. Jia, M.; Hong, S.; Wu, T.-S.; Li, X.; Soo, Y.-L.; Sun, Z. Single Sb sites for efficient electrochemical CO_2 reduction. *Chem. Commun.* **2019**, *55*, 12024–12027. [CrossRef]
11. Sarfraz, S.; Garcia-Esparza, A.T.; Jedidi, A.; Cavallo, L.; Takanabe, K. Cu-Sn Bimetallic Catalyst for Selective Aqueous Electroreduction of CO_2 to CO. *ACS Catal.* **2016**, *6*, 2842–2851. [CrossRef]
12. Zeng, J.; Bejtka, K.; Ju, W.; Castellino, M.; Chiodoni, A.; Sacco, A.; Farkhondehfal, M.A.; Hernández, S.; Rentsch, D.; Battaglia, C.; et al. Advanced Cu-Sn foam for selectively converting CO_2 to CO in aqueous solution. *Appl. Catal. B Environ.* **2018**, *236*, 475–482. [CrossRef]
13. Morimoto, M.; Takatsuji, Y.; Yamasaki, R.; Hashimoto, H.; Nakata, I.; Sakakura, T.; Haruyama, T. Electrodeposited Cu-Sn Alloy for Electrochemical CO_2 Reduction to CO/HCOO−. *Electrocatalysis* **2018**, *9*, 323–332. [CrossRef]
14. Ju, W.; Zeng, J.; Bejtka, K.; Ma, H.; Rentsch, D.; Castellino, M.; Sacco, A.; Pirri, C.F.; Battaglia, C. Sn-Decorated Cu for Selective Electrochemical CO_2 to CO Conversion: Precision Architecture beyond Composition Design. *ACS Appl. Energy Mater.* **2019**, *2*, 867–872. [CrossRef]
15. Yoo, C.J.; Dong, W.J.; Park, J.Y.; Lim, J.W.; Kim, S.; Choi, K.S.; Ngome, F.O.O.; Choi, S.-Y.; Lee, J.-L. Compositional and Geometrical Effects of Bimetallic Cu–Sn Catalysts on Selective Electrochemical CO_2 Reduction to CO. *ACS Appl. Energy Mater.* **2020**, *3*, 4466–4473. [CrossRef]
16. Dong, W.J.; Lim, J.W.; Hong, D.M.; Park, J.Y.; Cho, W.S.; Baek, S.; Yoo, C.J.; Kin, W.; Lee, J.-L. Evidence of Local Corrosion of Bimetallic Cu-Sn Catalysts and Its Effects on the Selectivity of Electrochemical CO_2 Reduction. *ACS Appl. Energy Mater.* **2020**, *3*, 10568–10577. [CrossRef]
17. Li, M.; Tian, X.; Garg, S.; Rufford, T.E.; Zhao, P.; Wu, Y.; Yago, A.J.; Rudolph, V.; Wang, G. Modulated Sn Oxidation States over a Cu_2O-Derived Substrate for Selective Electrochemical CO_2 Reduction. *ACS Appl. Mater. Interfaces* **2020**, *12*, 22760–22770. [CrossRef]
18. Singh, M.R.; Clark, E.L.; Bell, A.T. Effects of electrolyte, catalyst, and membrane composition and operating conditions on the performance of solar-driven electrochemical reduction of carbon dioxide. *PCCP* **2015**, *17*, 18924–18936. [CrossRef]
19. Nguyen, T.N.; Dinh, C.-T. Gas diffusion electrode design for electrochemical carbon dioxide reduction. *Chem. Soc. Rev.* **2020**, *49*, 7488–7504. [CrossRef]
20. Rabiee, H.; Ge, L.; Zhang, X.; He, S.; Li, M.; Yuan, Z. Gas diffusion electrodes (GDEs) for electrochemical reduction of carbon dioxide, carbon monoxide, and dinitrogen to value-added products: A review. *Energy Environ. Sci.* **2021**, *14*, 1959–2008. [CrossRef]
21. Zeng, J.; Bejtka, K.; Di Martino, G.; Sacco, A.; Castellino, M.; Re Fiorentin, M.; Risplendi, F.; Farkhondehfal, M.A.; Hernández, S.; Cicero, G.; et al. Microwave-Assisted Synthesis of Copper-Based Electrocatalysts for Converting Carbon Dioxide to Tunable Syngas. *ChemElectroChem* **2020**, *7*, 229–238. [CrossRef]
22. Knödler, H. On the Crystal Structure and Structure Relationships of the γ and ε Phases in the Cu-Sn System. *Metall* **1966**, *20*, 823–829.
23. Arnberg, L.; Jönsson, A.; Westman, S. The Structure of the delta-Phase in the Cu–Sn System. A Phase of gamma-Brass Type with an 18 Å Superstructure. *Acta Chem. Scand. Ser. A* **1976**, *30*, 187–192. [CrossRef]
24. Yuan, Z.; Zhang, Y.; Chen, H.; Xu, C. CTAB-assisted synthesis of eight-horn-shaped Cu_2O crystals via a simple solution approach. *J. Mater. Sci. Mater. Electron.* **2018**, *29*, 4256–4260. [CrossRef]
25. Chang, Y.; Zeng, H.C. Manipulative Synthesis of Multipod Frameworks for Self-Organization and Self-Amplification of Cu_2O Microcrystals. *Cryst. Growth Des.* **2004**, *4*, 273–278. [CrossRef]
26. Biesinger, M. Advanced analysis of copper X-ray photoelectron spectra. *Surf. Interface Anal.* **2017**, *49*, 1325–1334. [CrossRef]
27. Garino, N.; Zeng, J.; Castellino, M.; Sacco, A.; Risplendi, F.; Re Fiorentin, M.; Bejtka, K.; Chiodoni, A.; Salomon, D.; Segura-Ruiz, J.; et al. Facilely synthesized nitrogen-doped reduced graphene oxide functionalized with copper ions as electrocatalyst for oxygen reduction. *NPJ 2D Mater. Appl.* **2021**, *5*, 2. [CrossRef]
28. Zhang, B.A.; Ozel, T.; Elias, J.S.; Costentin, C.; Nocera, D.G. Interplay of homogeneous reactions, mass transport, and kinetics in determining selectivity of the reduction of CO_2 on Gold electrodes. *ACS Cent. Sci.* **2019**, *5*, 1097–1105. [CrossRef] [PubMed]
29. Vasileff, A.; Zhi, X.; Xu, C.; Ge, L.; Jiao, Y.; Zheng, Y.; Qiao, S.-Z. Selectivity control for electrochemical CO_2 reduction by charge redistribution on the surface of copper alloys. *ACS Catal.* **2019**, *9*, 9411−9417. [CrossRef]
30. Wang, P.; Qiao, M.; Shao, Q.; Pi, Y.; Zhu, X.; Li, Y.; Huang, X. Phase and structure engineering of copper tin heterostructures for efficient electrochemical carbon dioxide reduction. *Nat. Commun.* **2018**, *9*, 4933. [CrossRef] [PubMed]
31. König, M.; Vaes, J.; Klemm, E.; Pant, D. Solvents and Supporting Electrolytes in the Electrocatalytic Reduction of CO_2. *iScience* **2019**, *19*, 135–160. [CrossRef] [PubMed]
32. Dunwell, M.; Lu, Q.; Heyes, J.M.; Rosen, J.; Chen, J.G.; Yan, Y.; Jiao, F.; Xu, B. The central role of bicarbonate in the electrochemical reduction of carbon dioxide on gold. *J. Am. Chem. Soc.* **2017**, *139*, 3774–3783. [CrossRef] [PubMed]
33. Li, Q.; Fu, J.; Zhu, W.; Chen, Z.; Shen, B.; Wu, L.; Xi, Z.; Wang, T.; Lu, G.; Zhu, J.J.; et al. Tuning Sn-Catalysis for Electrochemical Reduction of CO_2 to CO via the Core/Shell Cu/SnO_2 Structure. *J. Am. Chem. Soc.* **2017**, *139*, 4290–4293. [CrossRef] [PubMed]
34. Ju, W.; Jiang, F.; Ma, H.; Pan, Z.; Zhao, Y.-B.; Pagani, F.; Rentsch, D.; Wang, J.; Battaglia, C. Electrocatalytic Reduction of Gaseous CO_2 to CO on Sn/Cu-Nanofiber-Based Gas Diffusion Electrodes. *Adv. Energy Mater.* **2019**, *9*, 1901514. [CrossRef]

35. Wang, J.; Ji, Y.; Shao, Q.; Yin, R.; Guo, J.; Li, Y.; Huang, X. Phase and structure modulating of bimetallic CuSn nanowires boosts electrocatalytic conversion of CO_2. *Nano Energy* **2019**, *59*, 138–145. [CrossRef]
36. Li, C.W.; Kanan, M.W. CO_2 Reduction at Low Overpotential on Cu Electrodes Resulting from the Reduction of Thick Cu_2O Films. *J. Am. Chem. Soc.* **2012**, *134*, 7231–7234. [CrossRef] [PubMed]
37. Coelho, A.A. TOPAS and TOPAS-Academic: An optimization program integrating computer algebra and crystallographic objects written in C++. *J. Appl. Cryst.* **2018**, *51*, 210–218. [CrossRef]